Chapter 6

RETRIEVAL OF OCEANIC CONSTITUENTS CONCENTRATIONS IN CASE II WATERS FROM MERIS DATA

6.1. Background

As described in Chapter 1, there are two challenges for atmospheric correction which need to be resolved. One concerns the atmospheric correction over turbid waters, the other concerns the atmospheric correction for atmospheres with strong-absorbing aerosols over both clear and turbid waters.

In Chapters 3 and 5, the oceanic constituents concentrations (CHL, SPM and CDOM) are successfully derived from ocean colour measurements at the sea level with ANN based on RT simulations. In this chapter, the same methodology is used to derive the oceanic constituents concentrations from ocean colour measurements at the top of atmosphere.

In this study, the light field in the atmosphere-ocean system at top of atmosphere is simulated by the radiative transfer code MOMO. The inherent optical properties of the oceanic constituents are the same as used in Chapter 5. In the atmosphere, various aerosols are considered, including maritime, continental, soot, dust as well as H_2SO_4. The simulated light field at the top of atmosphere is taken as the training data set for the ANN used for the retrieval of oceanic constituents. Input to the ANN is the remote sensing reflectance and other auxiliary parameters.

6.2. Simulated Data Sets

In the frame of this thesis, simulated data sets are used to derive the algorithms for the retrieval of oceanic constituent concentrations from reflectances at top of atmosphere. The inputs of radiative transfer simulations: IOPs and vertical distributions of the constituents in ocean and atmosphere, are described in the following subsections.

6.2.1. Atmosphere

The following atmospheric constituents are considered: air (molecular scattering) and aerosols (scattering and absorption). Other atmospheric constituents (clouds, absorbing gases, rain) are neglected.

6.2.1.1. Rayleigh Scattering

The vertical profile of molecular scattering is taken from *Elterman* (1968). The total optical thickness at a specific pressure p is computed from the approximation given by *Hansen and Travis* (1974):

$$\tau_r = \frac{p}{P_0}(8.524\times e^{-3}\lambda^{-4} + 9.63\times e^{-5}\lambda^{-6} + 1.1\times e^{-7}\lambda^{-8}), \quad (6.1)$$
$$where \;\; P_0 = 1013.25\, hPa$$

6.2.1.2. Aerosols

The basic constituents of aerosols are the following:

(a). oceanic particles (sea salt solution in water),

(b). water soluble particles,

(c). dust-like particles,

(d). Asian dust particles,

(e). soot particles,

(f). sulphuric acid solution in water.

Five aerosol models have been defined (listed in Table 6.1). The corresponding size distributions are listed in Table 6.2 [*Shettle and Fenn*, 1979; *WCRP*, 1986; *Fukushima and Toratami*, 1997].

Table 6.1 Aerosol models used in this study

Aerosol model	Constituent	Proportion (%)	Reference
Maritime	Rural aerosol mixtures (70% water soluble, and 30% dust-like particles) Oceanic	99 1	Shettle and Fenn, 1979
Continental	Water soluble Dust-like Soot	93.876 $2.27*10^{-4}$ 6.123	WCRP, 1986
Dust	Asian dust	100	Fukushima and Toratani, 1997
Soot	Soot	100	WCRP, 1986
H_2SO_4	75% solution of sulphuric acid in water	100	WCRP, 1986

The log-normal distribution is expressed as:

$$\frac{dN(r)}{d(\log(r))} = \frac{N_0}{\log(\delta)\sqrt{2\pi}} e^{-\frac{\log^2(r/r_b)}{2[\log(\delta)]^2}} \tag{6.2}$$

The modified Gamma function is expressed as:

$$\frac{dN(r)}{dr} = a\, r^{\alpha} e^{-b\, r^{\gamma}} \tag{6.3}$$

Here N(r) is the number of particles having radii smaller than r, r_b represents the mode radius, and δ represents the standard deviation.

Based on the above parameters, phase function (Figure 6.1), extinction coefficient (Figure 6.2), and single scattering albedo (Figure 6.3) are computed from Mie theory.

The vertical distribution of the aerosol is assumed as follows:

(1). Boundary layer (0 ~ 2 km): maritime, soot,

(2). Tropospheric layer (2 ~ 12 km): dust, continental

(3). Stratospheric layer (12 ~ 50 km): H_2SO_4.

Table 6.2 Size distributions of various aerosols used in this study

Type	Component	Size distribution			
		Log-normal			
		r0	σ		
Maritime_1	Rural_RH70	0.02846	2.238721		
	Oceanic_RH70	0.2041	2.511886		
Maritime_2	Rural_RH80	0.03274	2.238721		
	Oceanic_RH80	0.3180	2.511886		
Maritime_3	Rural_RH95	0.03884	2.238721		
	Oceanic_RH95	0.3803	2.511886		
Maritime_4	Rural_RH99	0.05215	2.238721		
	Oceanic_RH99	0.7505	2.511886		
Continental	Water soluble	0.005	2.99		
	Dust-like	0.5	2.99		
	Soot	0.0118	2.0		
Dust	Asian dust	0.40	3.00		
Soot	Soot	0.0118	2.00		
		Gamma modified			
		a	α	γ	b
H2SO4	75% H2SO4	324	1	1	18

6.2.2. Water

The considered water constituents and their IOPs models are the same as those described in Chapter 4. The following assumptions for the radiative transfer simulations in ocean are made:

- no vertical stratification of the ocean,
- the ocean is of infinite depth,
- no inelastic scattering inside the water body (*i.e.* no Raman scattering, no chlorophyll-a fluorescence, no CDOM fluorescence).

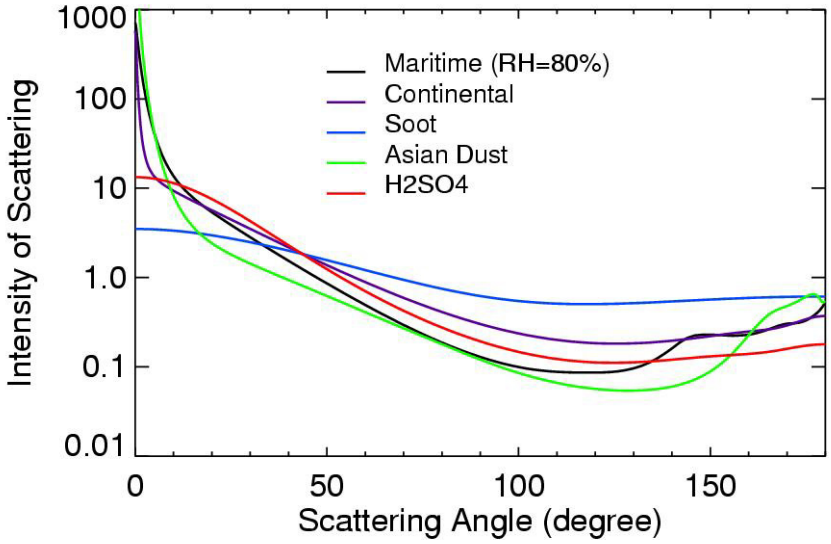

Figure 6.1. Phase functions of the aerosol models used in this study

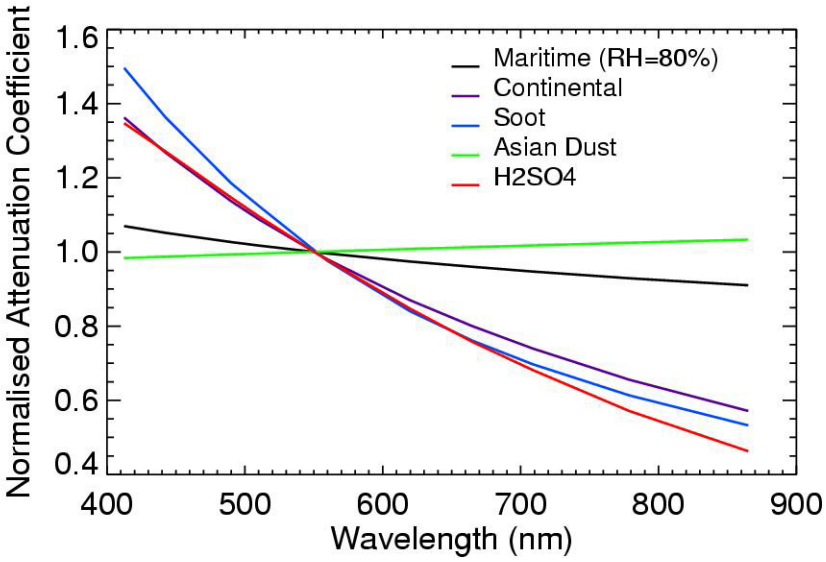

Figure 6.2. Normalised attenuation coefficients of the aerosol models used in this study

6.2.3. Sea Surface State

The rough sea surface is considered. The effects of the air-sea interface on the light field are introduced in the radiative transfer simulations by applying the statistic model of the wave surface distribution by *Cox & Munk* (1954), assuming a gaussian distribution of waves and a variable wind speed. The wind direction is not considered.

6.2.4. Ranges of the Related Parameters

Ranges of the oceanic constituent concentrations, optical thickness of various aerosols models at 550 nm, and other parameters used for the radiative transfer calculations are shown in Tables 6.3, 6.4 and 6.5, respectively.

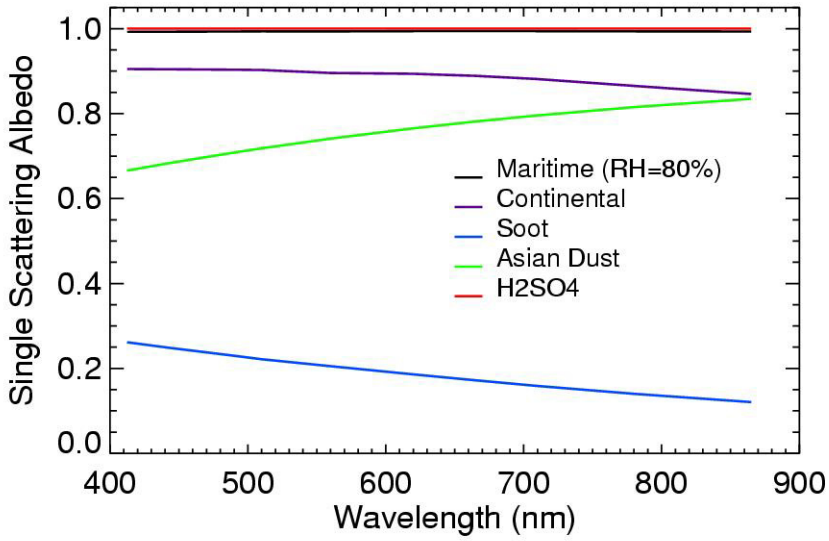

Figure 6.3. Single scattering albedo of the aerosol models used in this study

The wavelengths used in this study (Table 6.6) are the same as MERIS's wavelengths, but the following wavelengths are not included: 681.25 nm (chlorophyll fluorescence peak), 753.75 nm (cloud), 760.6 nm (O_2 absorption), 865 nm (water vapour reference), and 900 nm (water vapour absorption).

Table 6.3 Ranges of the oceanic constituents

Variable	Concentration unit	Min	Max
Pigment	mg/m^3	0.05	50
SPM	g/m^3	0.05	150
$a_y(443)$	m^{-1}	0.005	1.5

Table 6.4 Ranges of the atmospheric components

Aerosol model	Variable	Min	Max
Maritime	$\tau_a(550)$	0.01	0.5
Dust	$\tau_a(550)$	0.01	0.5
Soot	$\tau_a(550)$	0.001	0.1
Continental	$\tau_a(550)$	0.01	0.5
H2SO4	$\tau_a(550)$	0.005	0.005
Total aerosol	$\tau_a(550)$	0.065	1.0

Table 6.5. Ranges of geometric and other parameters

Variable	Unit	Min	Max
Solar zenith angle (θ_s)	degree	0.08	75.7
Obv. zenith angle (θ_v)	degree	0	41
Obv. azim. angle (ϕ_v)	degree	0	180
Surface air pressure (p)	hPa	1000	1040
Wind speed (w)	m/s	1	10

Table 6.6 Spectral channels and their bandwidths used in this study

MERIS Chan. No.	1	2	3	4	5	6	7	9	12	14
Center λ	412.5	442.5	490	510	560	620	665	709	779	885
Bandwidth	10	10	10	10	10	10	10	10	15	10

6.2.5. RT Simulations

The concentrations of the oceanic constituents for the RT simulations were selected according to the procedures described in Chapter 5. The optical thickness of the aerosols, the pressure at sea level, as well as the wind speed were selected randomly within the ranges defined in Tables 6.4 and 6.5. The relative humidity of the maritime aerosol was randomly distributed among the four values 70%, 80%, 95% and 99%.

Simulations of the remote sensing reflectance at the top of atmosphere were made for:

- 14 solar zenith angles between 0.08° and 75.6°,
- 9 observation zenith angles between 0° and 41.4°,
- 25 observation azimuth angles between 0° and 180°,

- 10 wavelengths: 412.5, 442.5, 490, 510, 560, 620, 665, 709, 779 and 885 nm,
- 2000 combinations of concentrations of three oceanic constituents, optical thickness of four aerosol models, pressures, as well as wind speed.

6.2.6. Creation of ANN Training Data Set

Following the simulation strategy described in section 6.2.5, for each of 2000 combinations, there are 14×9×25=3150 spectra which correspond to different observation geometries. Therefore, we have 2000×3150=6300000 spectra which can be used for ANN training. In practice, this number is too large to train ANNs due to limitations in memory and computing power. In this study, 20 of the 3150 spectra for each of the 2000 combinations were randomly taken as the training data.

Through adding noise to synthetic training data, the robustness of the trained ANN with respect to noisy input data is increased. In the present study, measurement errors exist more or less in all input parameters, e.g., radiometric calibration errors. Thus, it is necessary to add the appropriate noise to the data set used for the training of the ANNs to resist these measurement errors. The noise levels for different input parameters used in this study are listed in Table 6.7.

Table 6.7 The noise level added to training data inputs. The following acronyms are used: R1 to R10 represent the remote sensing reflectances at 10 wavelengths at TOA, 'W' represents the wind speed, 'a' represents the angles defined in Table 6.5, 'P' represents the pressure at sea level.

Parameter	R1	R2	R3	R4	R5	R6	R7	R8	R9	R10	W	a, P
Noise (%)	0.1	0.2	0.3	0.3	0.5	0.6	0.7	0.8	1.1	1.6	10	0.5

In order to reduce the complexity, a Rayleigh scattering correction was applied to the reflectance at the top of atmosphere. Here, no interaction between aerosol scattering and Rayleigh scattering was assumed. The algorithm for the Rayleigh scattering correction uses an ANN trained with radiative transfer calculations. The algorithm was developed according to the following procedures:

(1). Assuming black ocean and a rough sea surface for a pure Rayleigh atmosphere, 200 simulations corresponding to 200 different air pressures within the range 900 hPa to 1040 hPa were made.

(2). 150 of the 200 simulations were used to train a MLP ANN, the other 50 simulations were taken as validation data. The ANN consists of three layers: input layer, one hidden layer and output layer. The input layer consists of 6 neurons which correspond to the following parameters: pressure at the sea level, wind speed, as well as four geometric parameters: μ, x,

y, z (see below). The hidden layer consists of 30 neurons. The output layer consists of 10 neurons which correspond to remote sensing reflectances at TOA for 10 wavelengths.

(3). The ANN forecasts of remote sensing reflectances due to the contribution of Rayleigh scattering at top of atmosphere were compared to the corresponding reflectances resulting directly from RT simulations. The comparison results were shown in Figure 6.4 for training data set and validation data set. As shown in Figure 6.4, the remote sensing reflectances from the contributions of the Rayleigh scattering at TOA can be successful derived by the trained ANN.

6.3. Artificial Neural Networks

6.3.1. Structure of the ANN for Retrieval of the Constituents

In the present study, Multi-Layer Perceptrons (MLPs) ANN are used for the retrieval of the oceanic constituents from TOA data. The architecture of MLPs has been described in Section 2.4.

The retrieval of the oceanic constituents is based on the information contained in 15 parameters: Rayleigh-corrected remote sensing reflectances in 10 spectral channels at TOA: Rrs (412), Rrs(443), Rrsp(490), Rrs(510), Rrs(560), Rrs(620), Rrs(665), Rrs(709), Rrs(779), Rrs(885), wind speed, as well as the geometric parameters μ, x, y, and z, defined by *Schröder* (2003, personal communication):

$\mu=\cos(\theta_s)$

$x=\sin(\theta_v)\cos(\varphi)$

$y=\sin(\theta_v)\sin(\varphi)$

$z=\cos(\theta_v)$

A principal component analysis (PCA) was used to decorrelate all input parameters. As a result, the dimensionality of inputs to the ANN is reduced.

The output layer consists of 4 neurons which correspond to three oceanic constituents concentrations (CHL, SPM and CDOM) and total aerosol optical thickness at 550 nm. The hidden layer consists of 50 neurons.

6.3.2. Performance of the ANN-based Algorithm with Simulated Data

6.3.2.1. Performance with respect to the training data

40000 samples which have been generated according to the procedure described in Section 6.2.7 were used to train the ANN. The ANN-derived parameters were compared to the corresponding parameters used as input for the radiative transfer simulations (Figures 6.5, 6.6, 6.7 and 6.8 top of left panel for CHL, SPM, CDOM and $\tau_a(550)$, respectively). The calculated RMSE

and Pearson's correlation coefficient are listed in Table 6.8. As shown in these figures and Table 6.8, the inversion for the four parameters is successful with regard to the simulated training data.

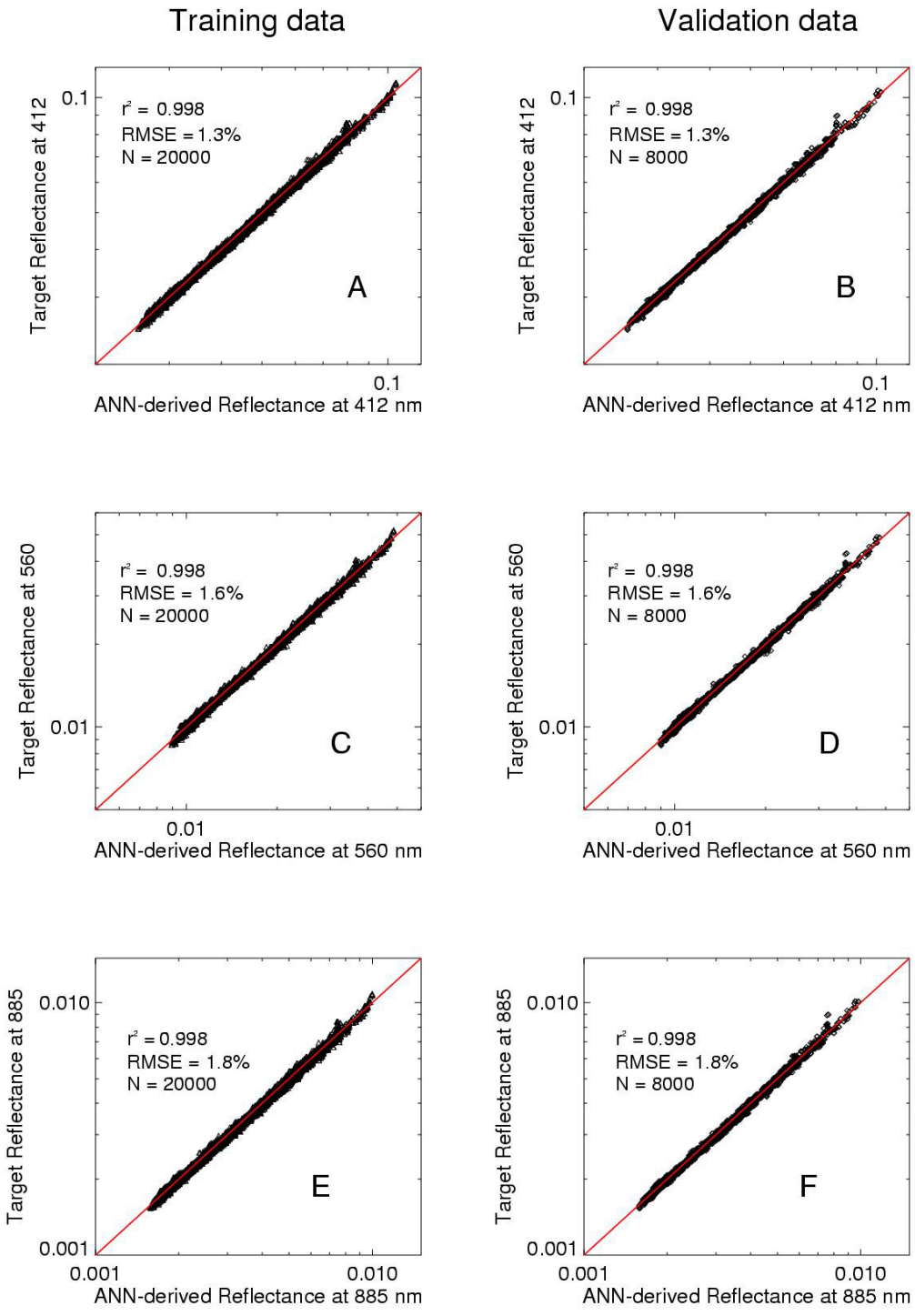

Figure 6.4. Scatter plot showing the performance of the ANN-based algorithm for the Rayleigh scattering correction. (A), (C) and (E) for the training data set at three wavelengths: 412 nm, 560 nm and 885 nm, respectively. (B), (D) and (F) for test data set at the same wavelengths.

Table 6.8. Performance of the ANN-based algorithm for the retrieval of the oceanic constituents as well as the optical thickness of aerosols

Data set	CHL		SPM		CDOM		Aerosol	
	r^2	RMSE (%)	r^2	RMSE (%)	r^2	RMSE (%)	r^2	RMSE (%)
Train	0.926	73.1	0.956	48.6	0.895	65.4	0.961	13.1
Test1	0.929	87.5	0.955	48.2	0.897	64.9	0.962	12.8
Test2	0.936	61.2	0.963	41.7	0.916	84.7	0.933	16.8
Test3	0.931	77.2	0.963	42.7	0.915	72.0	0.961	13.4
Test4	0.928	73.9	0.965	44.1	0.907	64.9	0.940	16.5
Test5	0.929	63.9	0.967	40.2	0.906	70.8	0.883	25.0
Test6	0.924	73.5	0.966	42.1	0.910	73.2	0.961	15.0
Test7	0.935	54.8	0.965	39.6	0.909	56.6	0.855	48.4

6.3.2.2 Performance with respect to the test data

In order to examine the performance of ANN-based algorithms for various atmospheric studies which may occur in the real environment, seven test data sets which correspond to different aerosol mixtures in the atmosphere were simulated (listed in Table 6.9). The inherent optical properties of the oceanic constituents used for simulations of test data sets are the same as used for the simulations of the training data set. Each test data set consists of 500 combinations of concentrations of three oceanic constituents, optical thickness of aerosols, air pressures, as well as wind speeds. The trained ANN was applied to these seven test data sets. The results are also, respectively, shown in Figures 6.5, 6.6, 6.7 and 6.8 for CHL, SPM, CDOM and $\tau_a(550)$, as well as listed in Table 6.8. Based on these results, the following conclusions can be drawn:

(1). With the trained ANN, the three oceanic constituents concentrations can be successfully derived from simulated reflectances at TOA for atmospheres ranging from weakly to strongly absorbing aerosols.

(2). With the trained ANN, the total optical thickness can be successfully derived for most cases except for TEST5 and TEST7. For both TEST5 and TEST7, the derived $\tau_a(550)$ is underestimated. TEST5 represents the most strongly absorbing aerosols, and TEST7 (Urban aerosol) is not included in the simulations of training data set. Although the retrieval of the total optical thickness for these two cases has a large error, it does not significantly impact the retrieval of oceanic constituents concentrations.

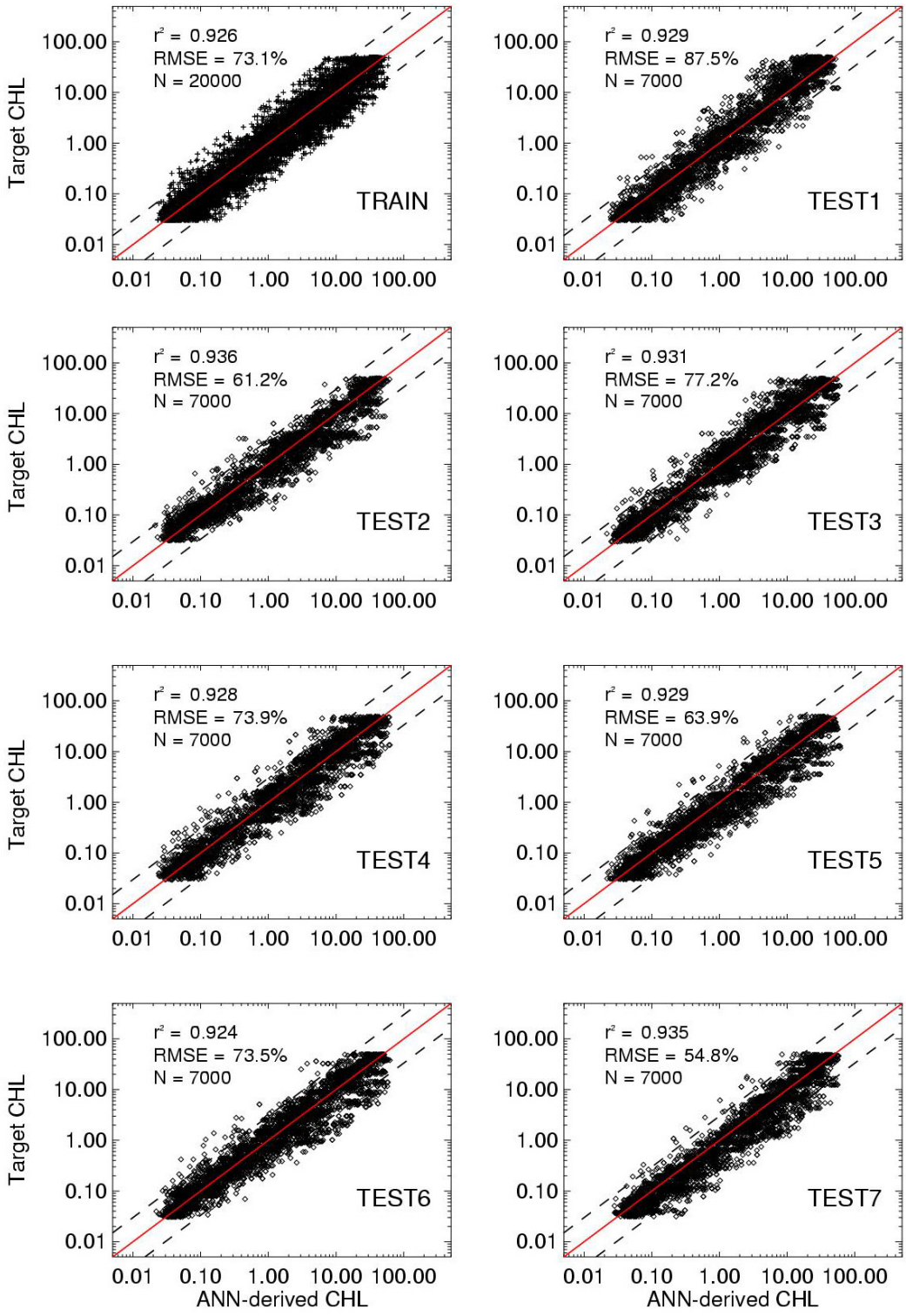

Figure 6.5. Scatter plot showing the performance of the ANN-based algorithm for pigment retrieval: training data set (top left panel, TRAIN), test data sets for seven different atmospheres (TEST1~TEST7). The target pigment concentration designates the pigment concentration used as input to the RT simulations. The dashed lines indicate the factor 3 error margin.

.

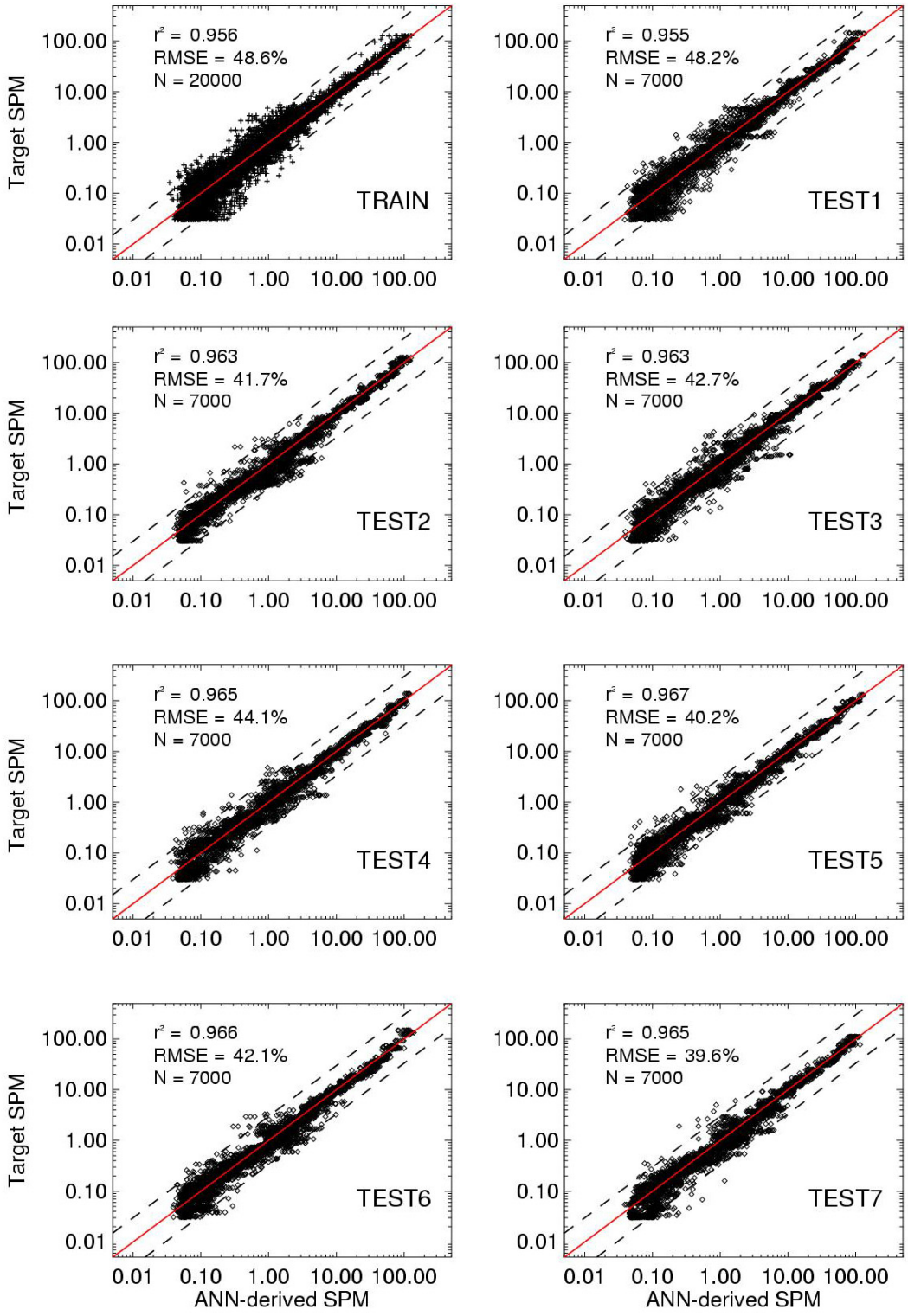

Figure 6.6. Scatter plot showing the performance of the ANN-based algorithm for SPM retrieval: training data set (top left panel, TRAIN), test data sets for seven different atmospheres (TEST1~TEST7). The target SPM concentration designates the SPM concentration used as input to the RT simulations. The dashed lines indicate the factor 3 error margin.

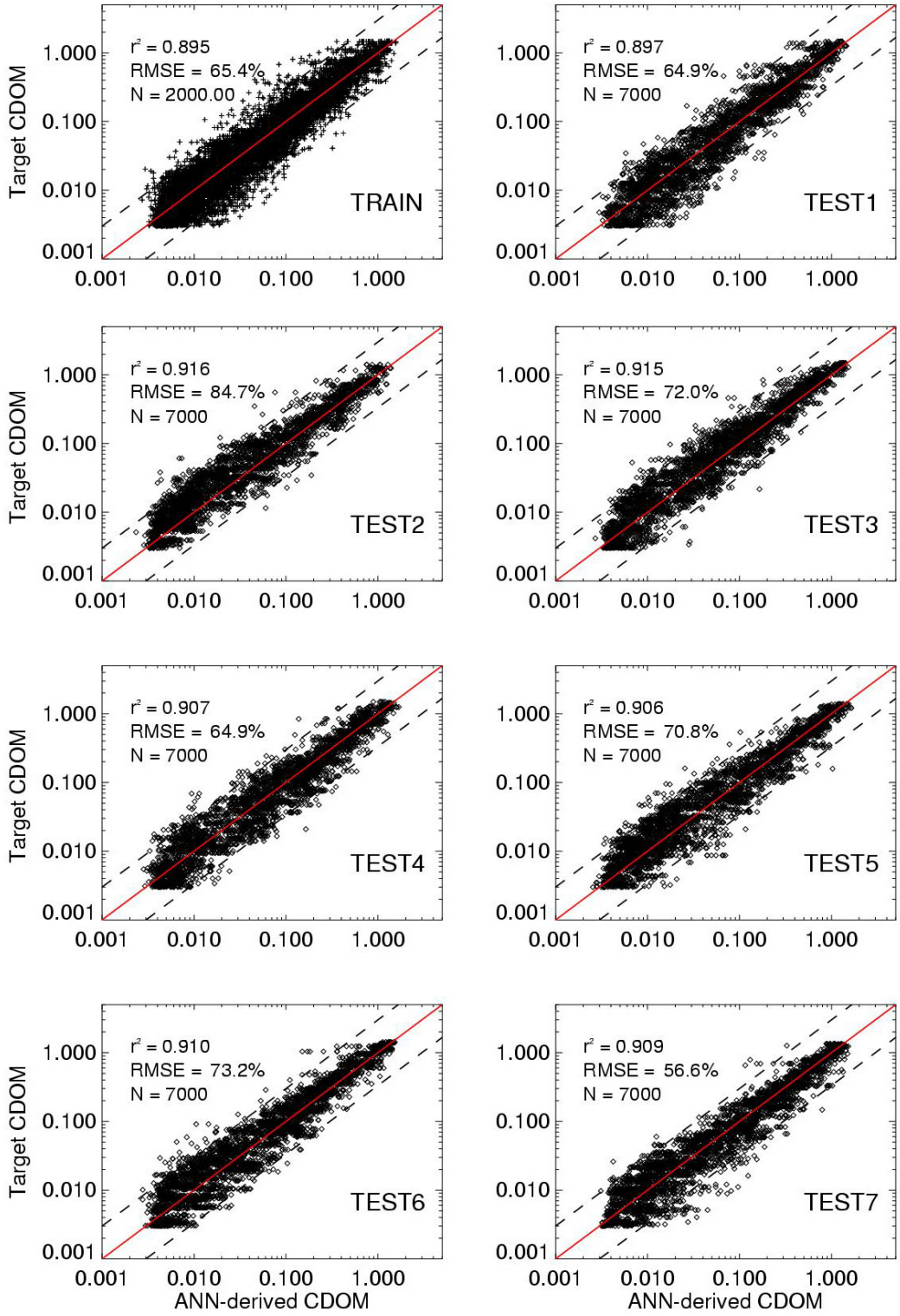

Figure 6.7. Scatter plot showing the performance of the ANN-based algorithm for CDOM retrieval: training data set (top left panel, TRAIN), test data sets for seven different atmospheres (TEST1~TEST7). The target CDOM absorption coefficient designates the CDOM absorption coefficients used as input to the RT simulations. The dashed lines indicate the factor 3 error margin.

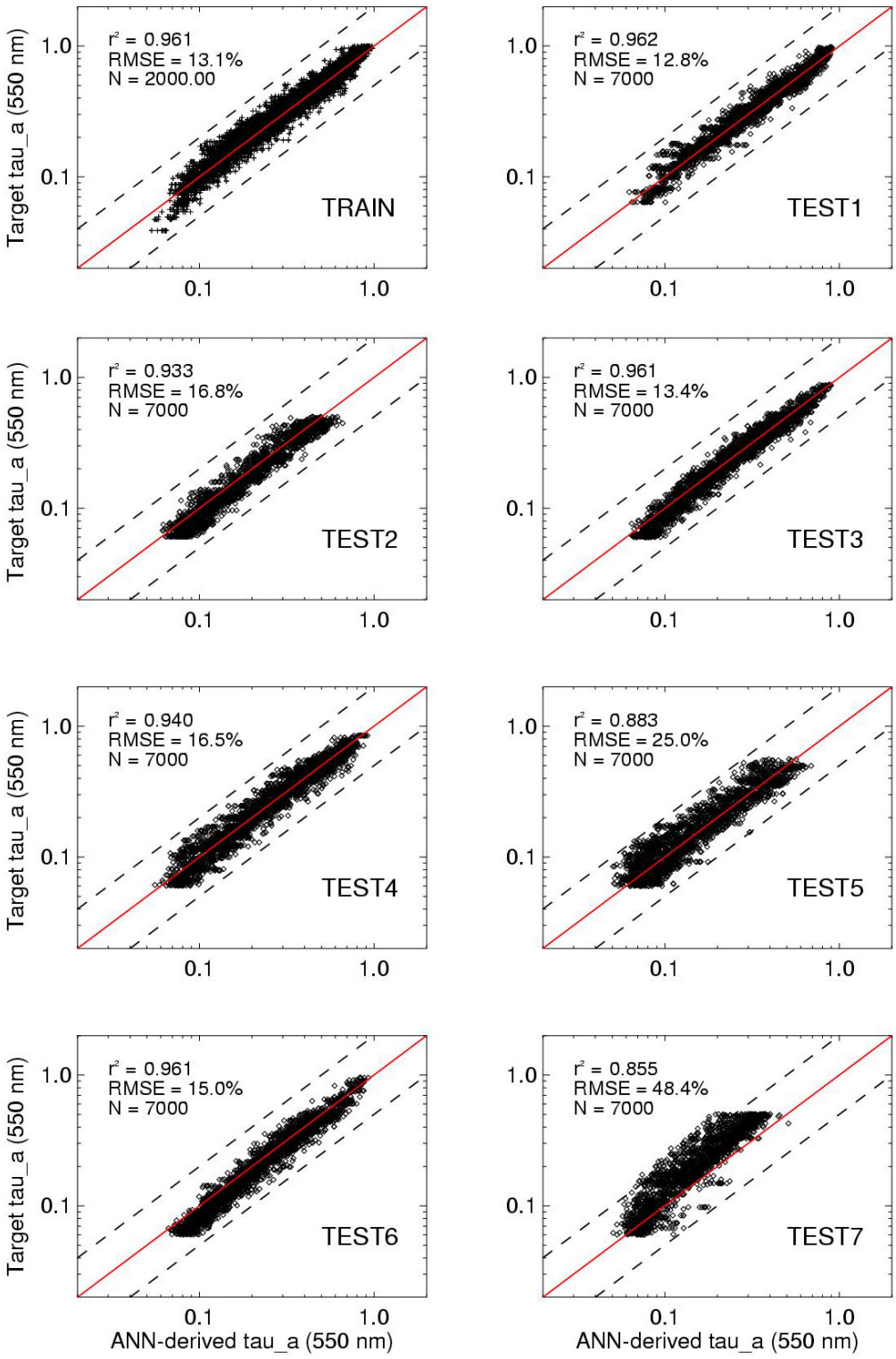

Figure 6.8. Scatter plot showing the performance of the ANN-based algorithm for aerosol optical thickness retrieval: training data set (top left panel, TRAIN), test data sets for seven different atmospheres (TEST1~TEST7). The target aerosol optical thickness designates the aerosol optical thickness used as input to the RT simulations. The dashed lines indicate the factor 2 error margin.

Table 6.9. Aerosol mixtures for testing the performance of the trained ANN

Test Data	Aerosol	Vertical Profile	Test Data	Aerosol	Vertical Profile
Test1	Maritime Soot Continental Asian dust H2SO4	0~2 km 0~2 km 2~12 km 2~12km 12~50 km	Test5	Maritime Soot H2SO4	0~2 km 0~2 km 12~50 km
Test2	Maritime H2SO4	0~2 km 12~50 km	Test6	Maritime Asian dust H2SO4	0~2 km 2~12km 12~50 km
Test3	Maritime Continental H2SO4	0~2 km 2~12 km 12~50 km	Test7	Urban H2SO4	0~2 km 12~50 km
Test4	Maritime Soot Asian dust H2SO4	0~2 km 0~2 km 2~12km 12~50 km			

6.4. Application to the MERIS Imagery

MERIS (Medium Resolution Imaging Spectrometer) has been launched on board the earth observation satellite ENVISAT on March 1, 2002. It has the following main specifications: spatial resolution of 300 m in full resolution mode, revisit period of 2-3 days, 15 programmable spectral bands with high radiometric sensitivity. These specifications are very suitable for monitoring water properties in coastal waters.

Two MERIS images were selected, which are located in the North Sea and the China Seas. Both the North Sea and the China Seas belong to Case II waters. The North Sea is greatly influenced by the Elbe, Weser, Ems, Rhine, and the Thames rivers. As a result, the concentrations of both SPM and CDOM are very high. Besides, the phytoplankton concentration is usually high due to a steady nutrient supply from the rivers and the atmosphere. The China Seas are greatly influenced by the discharge of Yellow River and Yangzi River. These two rivers are famous for their high SPM concentration: SPM values can exceed 100 mg/m^3 at the estuary of the two rivers [*Hu*, 2000; *Jiang et al*., 2002; *Wu et al*., 2003]. Besides, aerosols over the China Seas are characterised by their high variability in type and concentrations because of the presence of Asian dust particles as well as soot which originates from the main land of China [*Fukushima and Toratani*, 1997; *Li et al.,* 2002].

The ANN-based algorithm described in Section 6.3 was applied to the two selected images (Figures 6.9 and 6.15). The pigment concentration, SPM concentration, CDOM absorption coefficient at 443 nm, and total optical thickness of aerosols at 550 nm have been calculated. The results for the North Sea are shown in Figures 6.10, 6.11, 6.12 and 6.13 for CHL, SPM, CDOM and $\tau_a(550)$, respectively. The distribution of the derived parameters in the North Sea along a transect is depicted in Figure 6.14. Corresponding results for the China Seas are shown in Figures 6.16, 6.17, 6.18 and 6.19. The distribution of the derived parameters in the China Seas along a transect is depicted in Figure 6.20.

Since simultaneous *in-situ* measurements in these areas for the two selected images are not available, the derived results from the algorithm developed in this study can not directly be validated. Here, the following criteria to assess whether the derived results are reasonable.

(1). A low covariance between the distributions of SPM and aerosols.

By visual inspection, it becomes clear that the structures of the SPM distribution (Figure 6.11 and 6.17 for the North Sea and the China Seas, respectively) are different from the structures of the aerosol distribution (Figure 6.13 for the North Sea, Figure 6.19 for the China Seas), except for the area of Subei shoal and the mouth of Yellow River in the China Seas, where the concentrations of SPM are very high. This phenomenon can also clearly be seen from the distributions of SPM and aerosol along the same transect (Figure 6.14 for the North Sea, Figure 6.20 for the China Seas).

(2). The agreement of the distributions of the derived parameters with known distributions.

In the southern North Sea, the structure of the SPM distribution is very similar to that derived from CZCS imagery [*Doeffer and Fischer*, 1994]. A water band with high SPM concentration stretches from the Thames estuary at the southeast edge of Great Britain into the North Sea. Besides, CDOM shows the expected distribution in the mouth of the Elbe River, where a high CDOM band was found.

In the China Seas, SPM distribution shows the expected pattern in the mouth of Yellow River, in the Subei shoal, in the centre of Yellow Sea, as well as in the Bohai Strait. In the mouth of Yellow River, SPM concentration is very high due to the discharge of inorganic particles. In the Subei shoal, SPM concentration is also very high due to the re-suspended sediments. The centre of Yellow Sea is very clear and SPM concentrations are frequently found to be less than 0.5 g/m^3 [Ahn et al., 2001]. In the strait of the Bohai Sea, SPM concentration is relatively low due to the influence of Yellow Sea, from which a band of low SPM concentration stretches into the Bohai Sea [Jiang et al., 2002]. CDOM distributions in the Bohai Sea and around the mouth of Yangzi River are also within the expected pattern. In the Bohai Sea, CDOM is always high due to the discharge of Yellow River and waste water from factories. Around the mouth of Yangzi River, input of riverine waters causes high CDOM concentrations. The CHL concentrations in the Bohai Sea and around the outer path of Yangzi River plume are typically

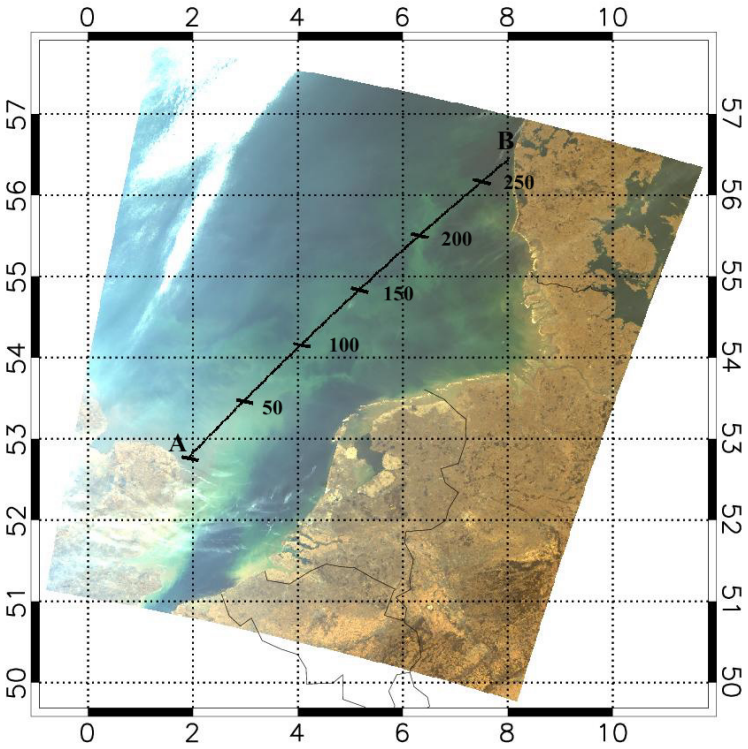

Figure 6.9. RGB image of MERIS above the North Sea (22 March, 2003). The black line indicates the transect used for further analysis.

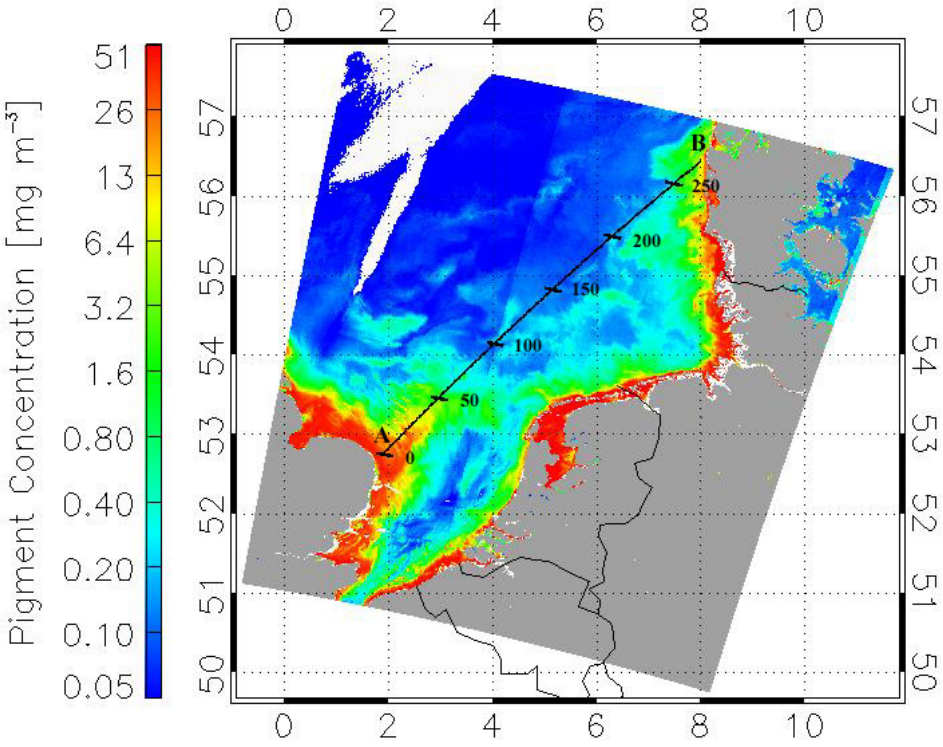

Figure 6.10. Pigment distribution derived from MERIS imagery for the North Sea (22 March, 2003)

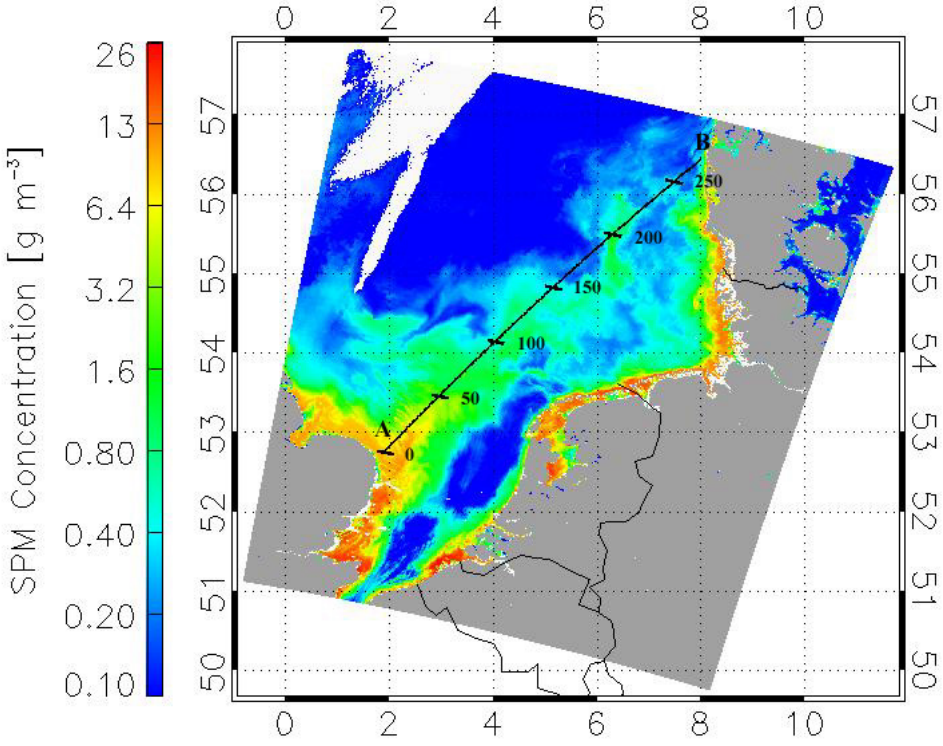

Figure 6.11. SPM distribution derived from MERIS imagery for the North Sea (22 March, 2003)

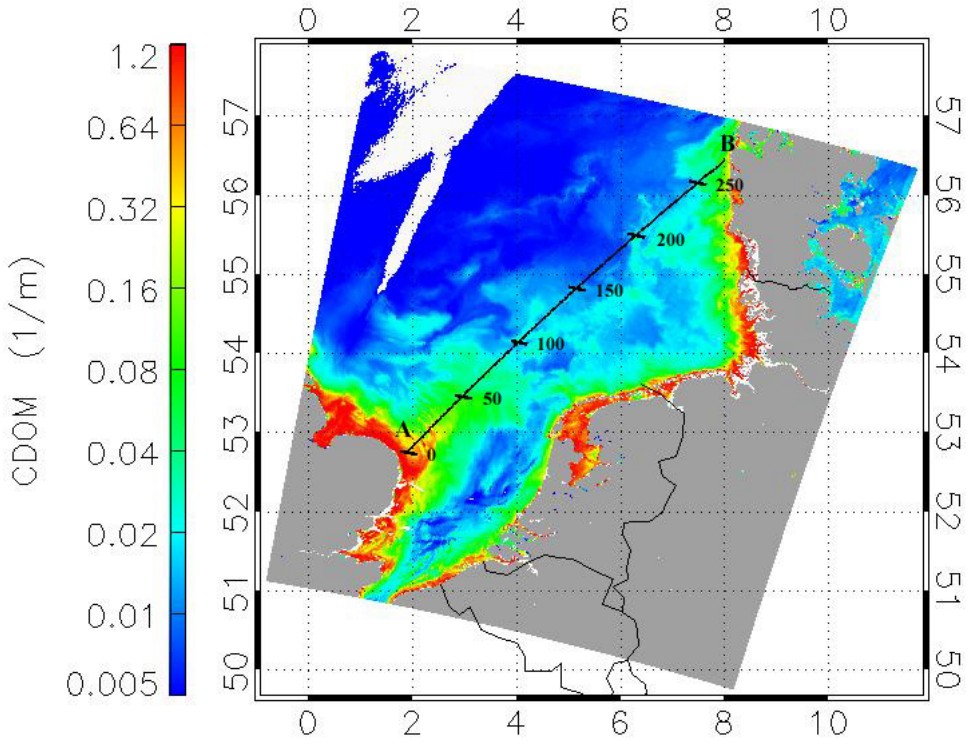

Figure 6.12. CDOM distribution derived from MERIS imagery for the North Sea (22 March, 2003)

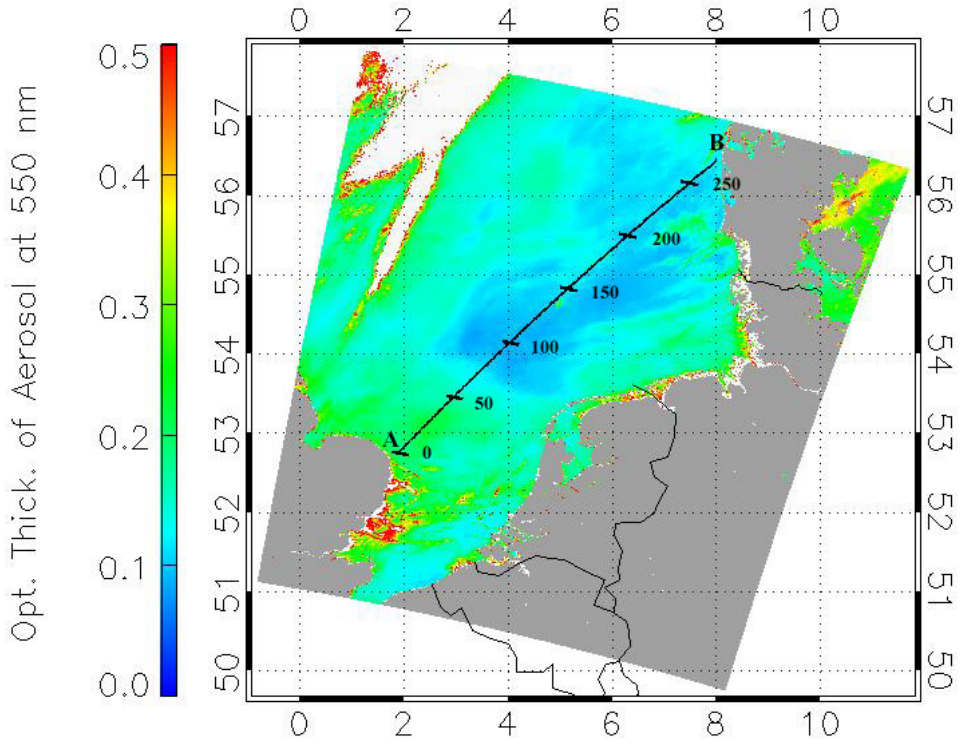

Figure 6.13. Aerosol distribution derived from MERIS imagery for the North Sea (22 March, 2003)

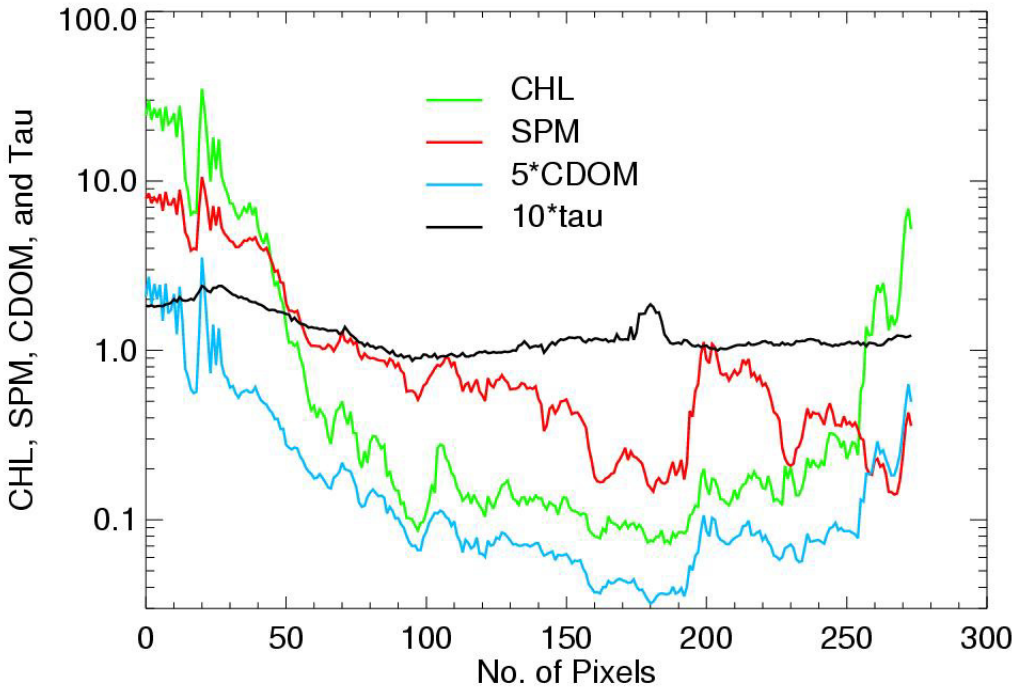

Figure 6.14. Distributions of pigment, SPM, CDOM and aerosol derived from MERIS imagery for the North Sea along the specfic transect (22 March, 2003)

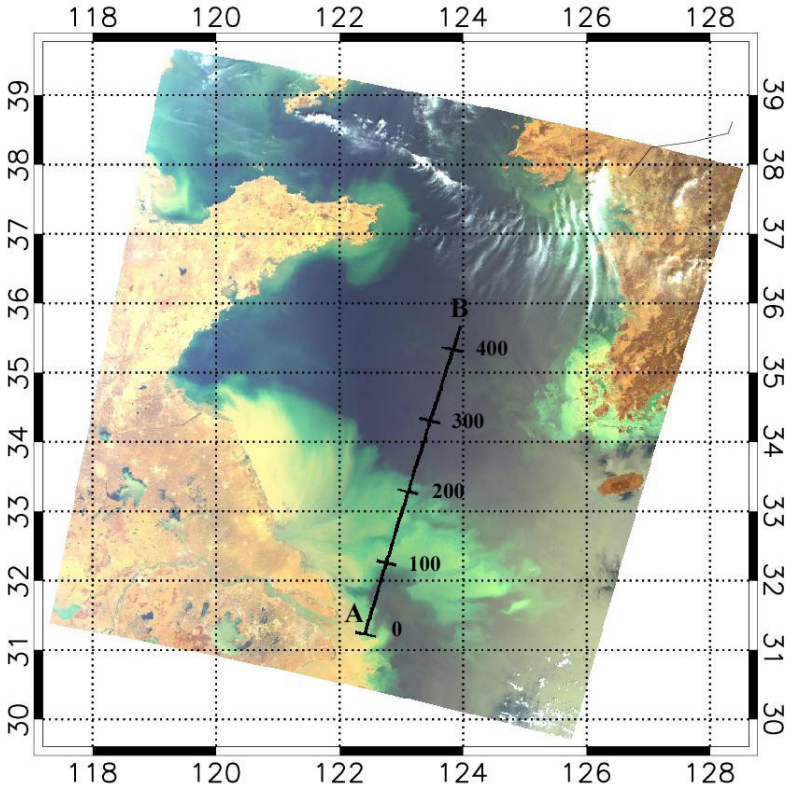

Figure 6.15. RGB image of MERIS above the China Seas (16 April, 2003). The black line indicates the transect used for further analysis

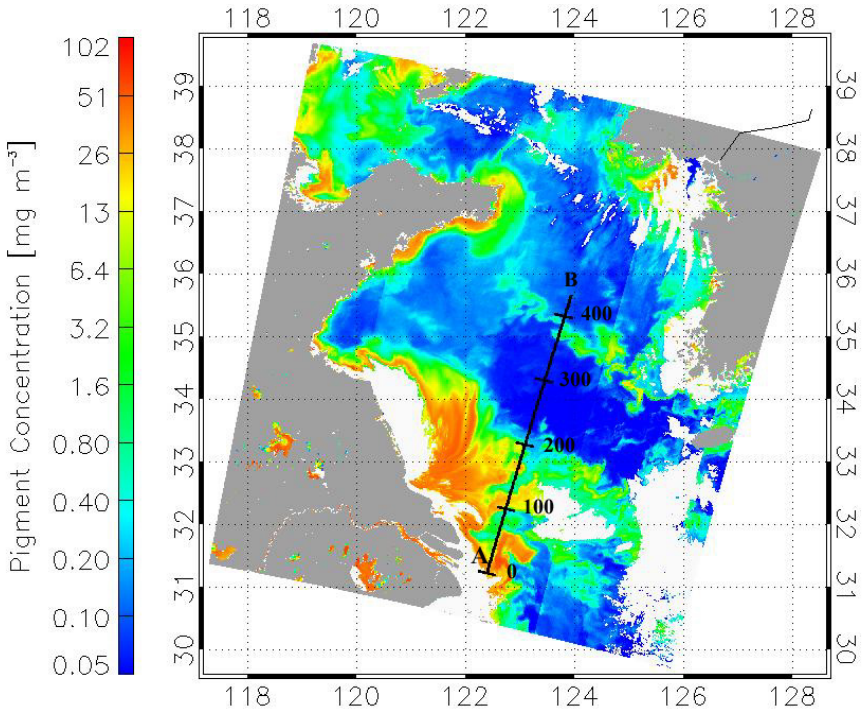

Figure 6.16. Pigment distribution derived from MERIS imagery for the China Seas (16 April, 2003)

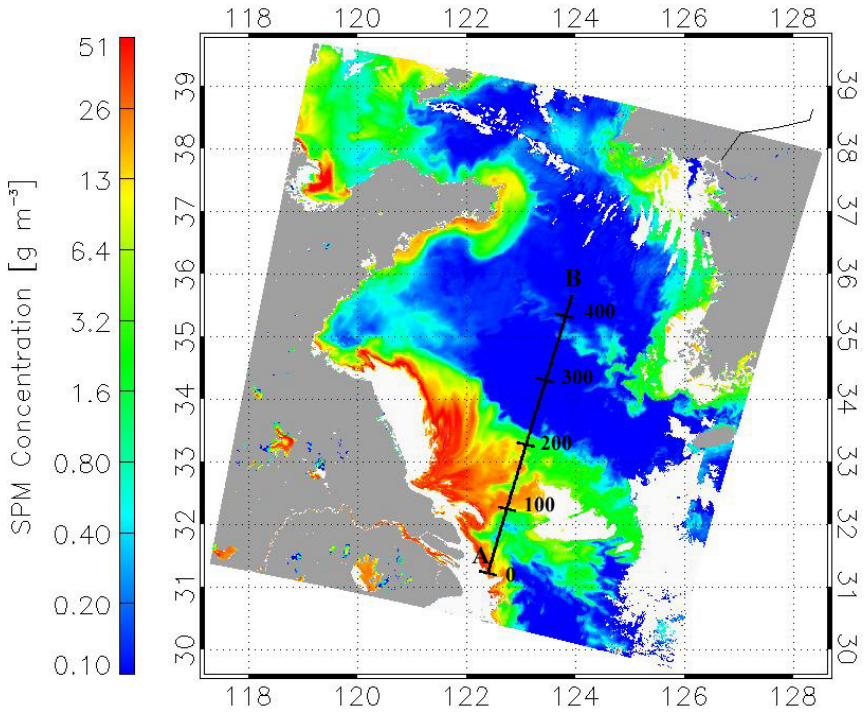

Figure 6.17. SPM distribution derived from MERIS imagery for the China Seas (16 April, 2003)

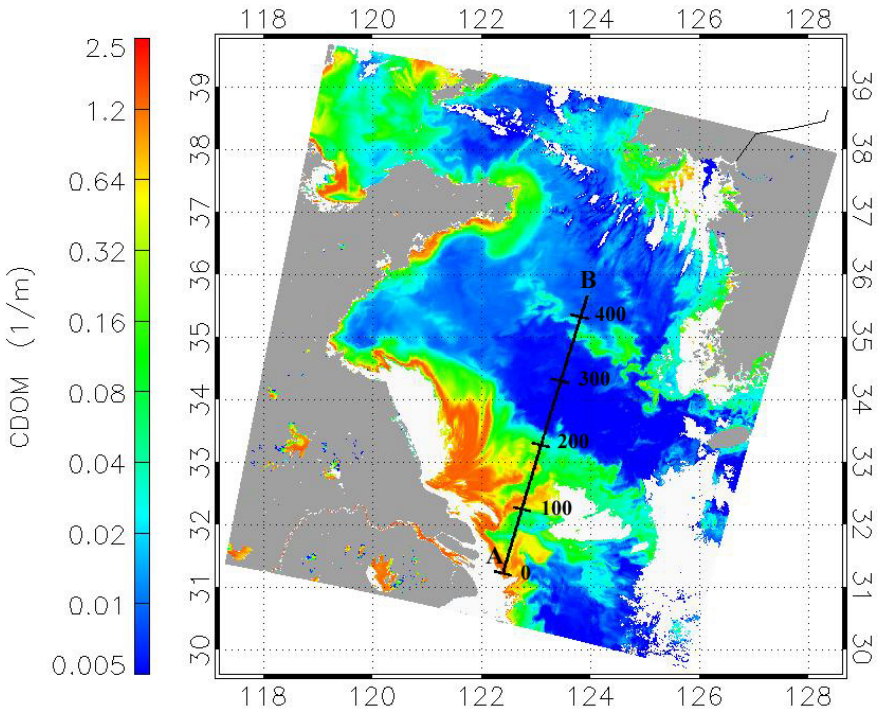

Figure 6.18. CDOM distribution derived from MERIS imagery for the China Seas (16 April, 2003)

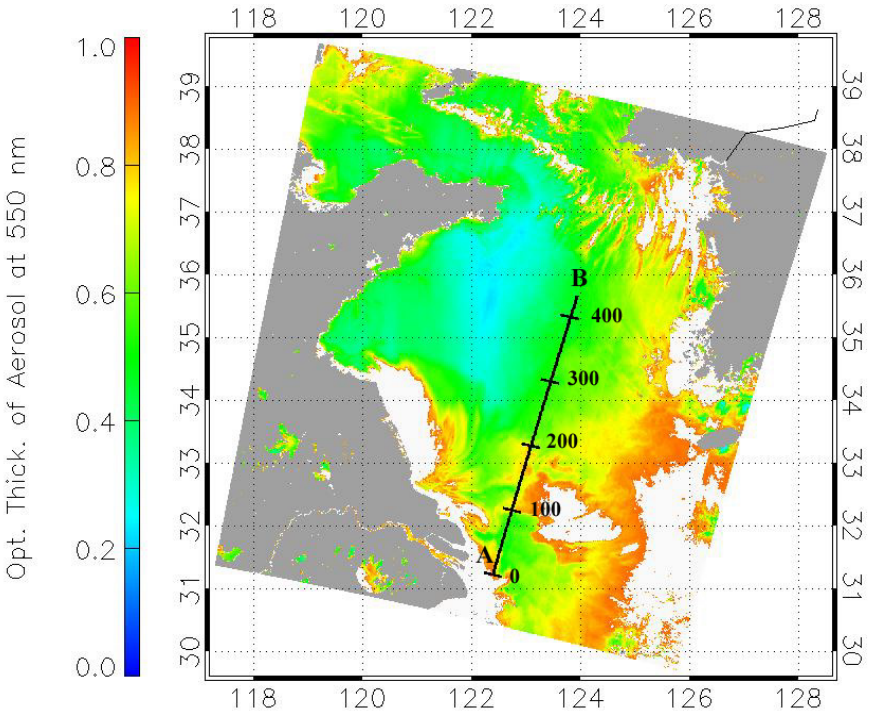

Figure 6.19. Aerosol distribution derived from MERIS imagery for the China Seas (16 April, 2003)

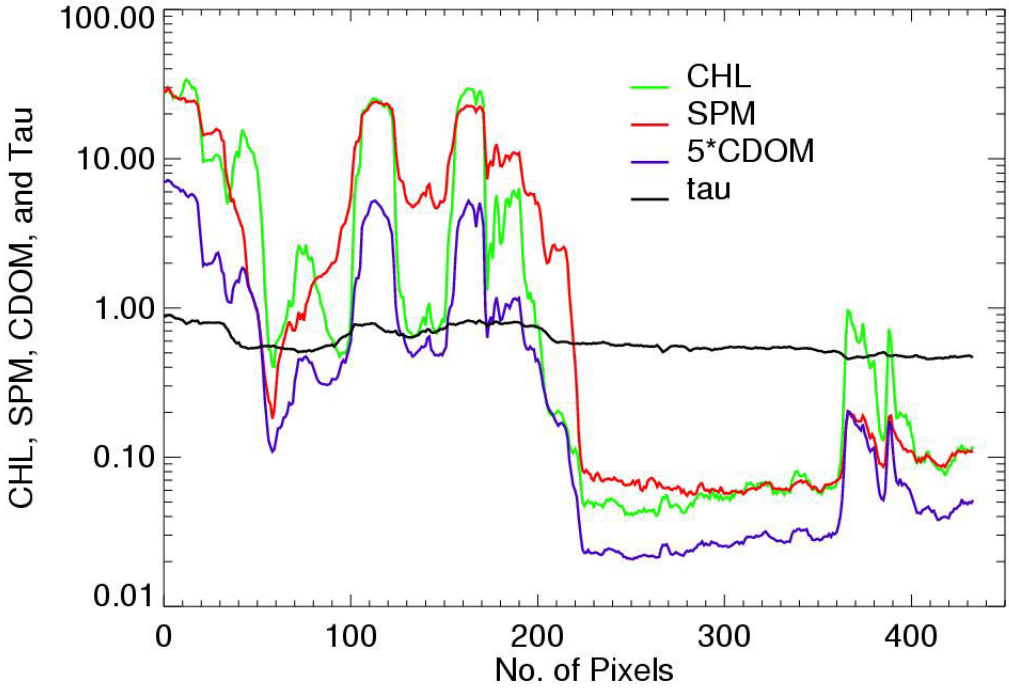

Figure 6.20. Distributions of pigment, SPM, CDOM and aerosol derived from MERIS imagery for the China Seas along the specfic transect (16 April, 2003).

higher than that in Yellow Sea. This distribution is also found in Figure 6.16. The range of derived SPM concentration is within the range known for the China Seas. The range of derived CHL concentration is also within the known range, except for the highly turbid waters. In the highly turbid waters, the derived CHL concentration is unreasonably high: around the Subei shoal and the mouth of Yangzi River, the derived CHL concentration exceeds 30 mg m^{-3}. In fact, although there is a rich nutrient supply in these areas, the availability of light is reduced due to the high SPM concentration. As a result, photosynthesis is reduced and the CHL concentration should be comparably low. The observed values in these areas are between 0.1 ~ 10 mg m^{-3} [Hu, 2000].

Judging from the above two criteria, the derived results seem to be reasonable except for the CHL retrieval in highly turbid waters of the China Seas. A possible reason for this is that the IOP models and the constraint conditions for the ranges of CHL, SPM and CDOM [Eq.(5.1) ~ (5.6)], used for development of the algorithm, are optimised for European waters. They may not be valid for some areas of the China Seas.

6.5. Conclusion

In this study, a methodology for the retrieval of three constituents from ocean colour at TOA above Case II waters have been derived. The retrieval method is derived by applying ANN techniques to a set of remote sensing reflectance spectra at TOA typical of Case II waters, which have been obtained from RT simulations.

The ANN employed in this study is a MLP with three layers: one input, one hidden and one output layer. A bias parameter is added both to the input layer and to the hidden layer. The input layer consists of 15 neurons which correspond to Rayleigh-corrected remote sensing reflectances of 10 wavelengths at TOA and other 5 auxiliary parameters. The hidden layer consists of 50 neurons. The output layer consists of four neurons which correspond to the concentrations of CHL, SPM and CDOM, as well as the total optical thickness of aerosols.

The ANN-based algorithm developed in this study seems to be a promising technique for the retrieval of oceanic constituents in Case II waters from ocean colour measurements at TOA. The examination of the performance of the ANN-based algorithm shows that it can deal with various atmospheres from weakly to strongly absorbing aerosols. Applied to the MERIS imagery of the North Sea and the China Seas, the results appears reasonable except for the highly turbid areas in the China Seas. Up to now, the algorithm has been tested for only a few images, and the validation is preliminary. In future, a more thorough validation of this algorithm using simultaneous *in-situ* measurements in different waters should be carried out. Besides, in order to optimise this method for the China Seas, precise information on the optical properties of oceanic constituents in the China Seas are required.